Reading the climate record of the martian polar layered deposits

C.S. Hvidberg [a,*], K.E. Fishbaugh [b], M. Winstrup [a], A. Svensson [a], S. Byrne [c], K.E. Herkenhoff [d]

[a] Centre for Ice and Climate, Niels Bohr Institute, University of Copenhagen, Juliane Maries Vej 30, DK-2100 Copenhagen, Denmark
[b] Center for Earth and Planetary Studies, Smithsonian National Air and Space Museum, Washington, DC 20013, USA
[c] Lunar and Planetary Laboratory, University of Arizona, 1629 East University Blvd., Tucson, AZ 85721-0092, USA
[d] United States Geological Survey, 2255 N. Gemini Drive, Flagstaff, AZ 86001-1698, USA

ARTICLE INFO

ABSTRACT

The martian polar regions have layered deposits of ice and dust. The stratigraphy of these deposits is exposed within scarps and trough walls and is thought to have formed due to climate variations in the past. Insolation has varied significantly over time and caused dramatic changes in climate, but it has remained unclear whether insolation variations could be linked to the stratigraphic record. We present a model of layer formation based on physical processes that expresses polar deposition rates of ice and dust in terms of insolation. In this model, layer formation is controlled by the insolation record, and dust-rich layers form by two mechanisms: (1) increased summer sublimation during high obliquity, and (2) variations in the polar deposition of dust modulated by obliquity variations. The model is simple, yet physically plausible, and allows for investigations of the climate control of the polar layered deposits (PLD). We compare the model to a stratigraphic column obtained from the north polar layered deposits (NPLD) (Fishbaugh, K.E., Hvidberg, C.S., Byrne, S., Russel, P.S., Herkenhoff, K.E., Winstrup, M., Kirk, R. [2010a]. Geophys. Res. Lett., 37, L07201) and show that the model can be tuned to reproduce complex layer sequences. The comparison with observations cannot uniquely constrain the PLD chronology, and it is limited by our interpretation of the observed stratigraphic column as a proxy for NPLD composition. We identified, however, a set of parameters that provides a chronology of the NPLD tied to the insolation record and consistently explains layer formation in accordance with observations of NPLD stratigraphy. This model dates the top 500 m of the NPLD back to ∼1 million years with an average net deposition rate of ice and dust of 0.55 mm a^{-1}. The model stratigraphy contains a quasi-periodic ∼30 m cycle, similar to a previously suggested cycle in brightness profiles from the NPLD (Laskar, J., Levrard, B., Mustard, F. [2002]. Nature, 419, 375–377; Milkovich, S., Head, J.W. [2005]. J. Geophys. Res. 110), but here related to half of the obliquity cycles of 120 and 99 kyr and resulting from a combination of the two layer formation mechanisms. Further investigations of the non-linear insolation control of PLD formation should consider data from other geographical locations and include radar data and other stratigraphic datasets that can constrain the composition and stratigraphy of the NPLD layers.

© 2012 Elsevier Inc. All rights reserved.

1. Introduction

The martian poles are covered by polar layered deposits (PLD) of ice and dust. The stratigraphy of these deposits is visible on images from space and has been observed for decades (Murray et al., 1972; Howard et al., 1982; Tanaka, 2005). It is believed that the layers formed due to climate modulated variations in the deposition rates of ice and dust, and that they are the geological expression of insolation variations on Mars (Clifford et al., 2000; Fishbaugh et al., 2008).

The obliquity and eccentricity of Mars have varied significantly in the past and caused large variations of insolation in the polar areas. Several studies have suggested how the quasi-periodic variations of the orbital parameters have affected martian climate over time and discussed how the polar deposition rates of ice and dust may have varied accordingly (Toon et al., 1980; Cutts and Lewis, 1982; Laskar et al., 2002; Levrard et al., 2007; Newman et al., 2005). However, while the insolation influence of climate and depositional processes appears inevitable, it has remained unclear whether the climate signal recorded in the stratigraphy can be interpreted and linked to variations of insolation.

We present here a new model of layer formation based on physical processes that expresses polar deposition rates of ice and dust in terms of insolation. We compare the model stratigraphy to a recently published quantitative stratigraphic column from the north polar layered deposits (NPLD) (Fishbaugh et al., 2010a), and determine model parameters by matching the model stratigraphy to the

observations. We discuss the limitations of the comparison, and propose further work to investigate the climate control of the PLD stratigraphy on Mars.

2. Background

During the last decades, knowledge of the martian polar layered deposits has increased significantly. Space missions to Mars have mapped the PLD and their stratigraphy, and investigated their composition. The NPLD form a several km thick dome over the North Pole that extends over hundreds of km with a maximum thickness above 2 km near the pole and gradual thinning towards the margins (Phillips et al., 2008). They consist mainly of water ice with less than 5% dust (Grima et al., 2009). The bright surface layers on the residual ice cap are very smooth and among the youngest on Mars and current resurfacing rates suggest recent or ongoing deposition with deposition rates in the order of mm/yr (Banks et al., 2010).

A system of spiraling troughs cut into the bright surfaces of the NPLD and reveal extensive layering on the equator-facing trough walls (Fig. 1). Layers have been followed in scarps over hundreds of km (Malin and Edgett, 2001), and sequences of visible layers have been correlated between trough walls (Fishbaugh and Hvidberg, 2006). Radar surveys have mapped the internal structure of the NPLD, and show that radar layers are laterally continuous and extend across the NPLD (Phillips et al., 2008). A recent study suggests that that the spiral troughs have been present during the build-up of the upper 500–700 m of the NPLD (Smith and Holt, 2010). The internal structure near troughs suggests that deposition has been draping north-facing and horizontal slopes while sublimation has been eroding south-facing slopes, resulting in a north-ward constructional trough migration that reveals the layer structure contemporaneously with buildup of layers (Howard et al., 1982; Smith and Holt, 2010).

Before searching for a climate signal in the stratigraphic record, it must be justified that the stratigraphy is likely to be controlled by the global climate on Mars, and is not a result of local or random processes. The continuous internal layering that extends across the

Fig. 1. Image mosaic showing (a) the NPLD and zooming in on (b) the polar trough and (c) visible layers considered in this work. (a and b) Portion of a MOC image (NASA/JPL/Malin Space Science Systems). (c) HiRISE image PSP_001738_2670 (NASA/JPL/University of Arizona). The white frame in (c) indicates the outline of the portion shown in Fig. 3. The image shows some local disturbance of the stratigraphy where the trough curves, but not affecting the stratigraphy in the white frame considered in this work.

NPLD as well as the upper layers whose stratigraphy is correlated between trough walls, suggest that the stratigraphy results from large scale atmospheric deposition. Even though the troughs cut through the upper ~500 m in the interior main part of the NPLD, the stratigraphy is preserved and layer thickness at the pole-ward side of the troughs appears unaffected (Smith and Holt, 2010). The overall shape of the NPLD has been largely explained by a sublimation model controlled by latitude-dependent insolation, suggesting that the overall buildup of the NPLD is controlled by insolation (Ivanov and Muhleman, 2000).

In the past, orbital and axial parameters of Mars have varied significantly and caused dramatic changes in insolation. The variation of orbital and axial parameters of Mars has been reliably calculated back to 10 million years ago (Ma) (Laskar et al., 2004). The most important features related to the polar insolation are the periodic oscillations of obliquity with a 120 thousand year (kyr) period, and the shift in average obliquity that occurred at about 5 Ma (Fig. 2). The precession cycle of about 51 kyr, and eccentricity cycles of 95–99 kyr and 2.4 Myr also influence the insolation record. Before 10 Ma, uncertainties lead to a chaotic behavior of the obliquity calculation, but studies suggest that the average obliquity over 5 Gyr was 35–40°, i.e. higher than the present value of 25.2° (Laskar et al., 2004).

Insolation variations at the North Pole must have influenced the evolution of the NPLD. Climate models have estimated that polar ice becomes unstable above a critical obliquity of 35–40° (Levrard et al., 2007). This study proposed that the NPLD formed after the obliquity shift at 5 Ma from a previously higher level with obliquity maxima of >45°. On the other hand, it has been proposed that dust lags at the surface of the NPLD could have protected it against erosion during high-obliquity periods, and the NPLD could be much older (Levrard et al., 2007; Tanaka et al., 2008). Unfortunately, the initial build-up of the NPLD is poorly constrained by geological data. The NPLD has formed above terrain dating back to 3–1 Ga, and subsequent ice-rich deposits are smooth due to deposition and sublimation processes making it impossible to determine their age from crater densities (Tanaka et al., 2008).

It has been very difficult to decipher the climate record from the stratigraphy of the martian polar layered deposits. Cutts and Lewis (1982) proposed physical models of deposition of ice and dust and simulated polar layer formation controlled by insolation, but the resolution of Viking images was not sufficient to test the model. Several studies have searched for periodic signals in visual brightness records obtained from Mars Orbiter Camera (MOC) images. Laskar et al. (2002) identified two frequencies in a visual brightness profile and related them to the precession and obliquity cycles. A characteristic cycle of ~30 m was identified in 27 images of troughs across the NPLD (Milkovich and Head, 2005; Milkovich et al., 2008), and attributed to the precession cycle. A later analysis of visual brightness profiles found no significant cycles at similar wavelengths, but identified quasi-periodic cycles of ~1.6 m within thinner layers (Perron and Huybers, 2009). Analyses of High Resolution Imaging Experiment (HiRISE) images have revealed that the visual appearance of layers is partially masked by a younger coating of dust and ice, suggesting that the relation between the visual brightness of layers and their internal composition is not simple (Herkenhoff et al., 2007; Fishbaugh et al., 2010b). Internal radar reflection layers are related to variations in dielectric properties within the NPLD, and thought to be dust rich (Phillips et al., 2008). The internal radar layers were proposed to relate to obliquity cycles, and their structure has been suggested to support a ~5 Myr age of the NPLD, but it is not clear what climate conditions favor formation of such layers (Phillips et al., 2008; Putzig et al., 2009).

Cutts and Lewis (1982) described how the challenge in decoding the climate signal of the martian polar layers is similar to the
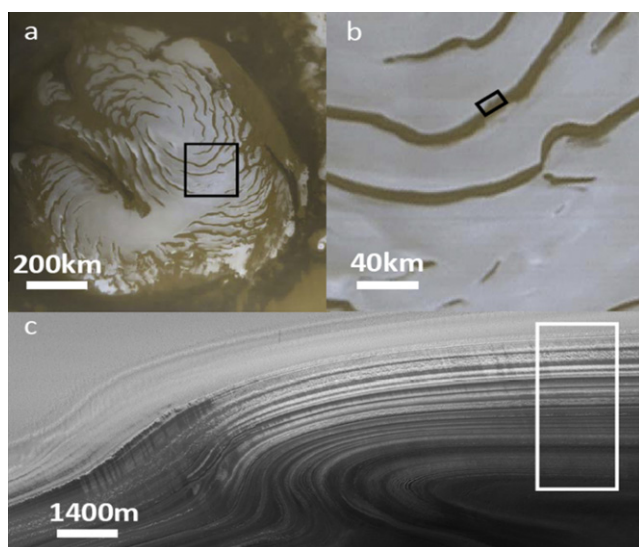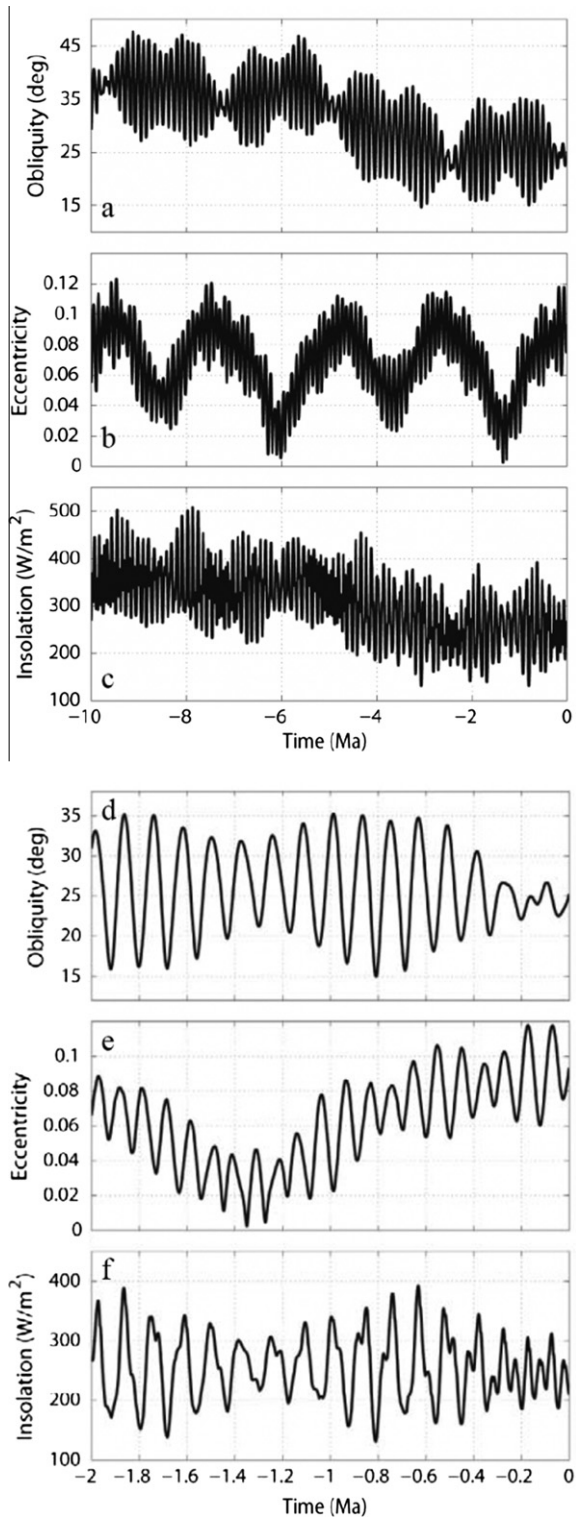
Fig. 2. Obliquity, eccentricity and insolation at the North Pole at summer solstice. (a–c) Over 10 Myr. (d–f) Over 2 Myr (Laskar et al., 2004).

from deep ocean cores and relied on two factors: (1) the timescale of the record was established with adequate accuracy, and (2) a chemical constituent of the sediment core (stable oxygen isotope ratio) could be directly related to temperature and ice sheet volume, thus establishing the link between the climate forcing and the sediment record.

Since no independent timescale of the NPLD formation is available, we will expand on ideas originally proposed by Cutts and Lewis (1982) by developing a more general model that considers variations of both ice and dust deposition rates controlled by insolation, and comparing the resulting record of ice and dust composition with present observations of NPLD stratigraphy.

3. Stratigraphic data

Images from the HiRISE instrument now document the stratigraphy of the NPLD in very high resolution (~30 cm/pixel) (Herkenhoff et al., 2007). The images show a complex stratigraphy of dark and bright layers with thicknesses ranging from scales of 0.1–10 m.

3.1. A stratigraphic column

In this work, we use a high-resolution measured stratigraphic column from a trough at 87.1°N, 92.6°E, constructed from a stereo pair of HiRISE images PSP_001738_2670 and PSP_001871_2670 (Fishbaugh et al., 2010a). The stratigraphic column is divided into marker beds, sections of thin layers, and undifferentiated sections. Layer types are identified due to their morphology, and layer boundaries were measured on a digital elevation model (DEM) constructed from the stereo pair (Fishbaugh et al., 2010a).

Marker beds are prominent, erosionally resistant layers with a distinctive visual morphology. They have hummocky layer edges and pitting at their surfaces, and they often appear dark (Fishbaugh et al., 2010a). Thin layers are also erosionally resistant and occur in sections with multiple thin layers separated by less-resistant layers. Thin layers protrude from other layers and are relatively smooth (Fishbaugh et al., 2010a). Fig. 3 shows images and a shaded relief map of the trough wall with indications of marker beds and sections of thin layers.

The dataset consists of elevations of marker bed boundaries and elevations of thin layers (Fishbaugh et al., 2010a) (Fig. 4). Morphological layer boundaries were marked using the stereo pair and a shaded relief map constructed from the DEM (Fishbaugh et al., 2010a). Elevations of these layer boundaries were measured on the DEM. Layer boundaries are marked by major slope breaks in topographic profiles (Fishbaugh et al., 2010b), and the elevation of each boundary were obtained from an average of measurements over ~100 m along the layer boundary (Fishbaugh et al., 2010a). The thickness of marker beds could be resolved on the DEM, but only the elevation of thin layers was measured due to resolution limits.

The marker beds were proposed to be the geologic expression of the ~30 m cycle in brightness profiles (Milkovich and Head, 2005), and the separation distance between thin layers matched the ~1.6 m cycle (Perron and Huybers, 2009), but the analysis showed no simple cyclic layering within the stratigraphic column (Fishbaugh et al., 2010a).

3.2. A climate proxy interpreted from the stratigraphic column

The stratigraphic column provides a record of layers identified due to their erosional resistance, but it is not evident how it can be interpreted as a climate proxy. Erosional resistance may depend both on internal layer properties, such as density and composition of ice and dust, and on conditions at the exposed layer surface. The

first attempts to demonstrate the astronomical climate theory for Earth: On Earth, variations in the orbital and axial parameters are on the order of 2° and much smaller than those on Mars, yet the terrestrial ice ages, with continental-scale ice sheets forming and retreating in the Northern Hemisphere, have been linked to astronomical forcing of climate on Earth (Hays et al., 1976). The relation for Earth was demonstrated in sediment records obtained
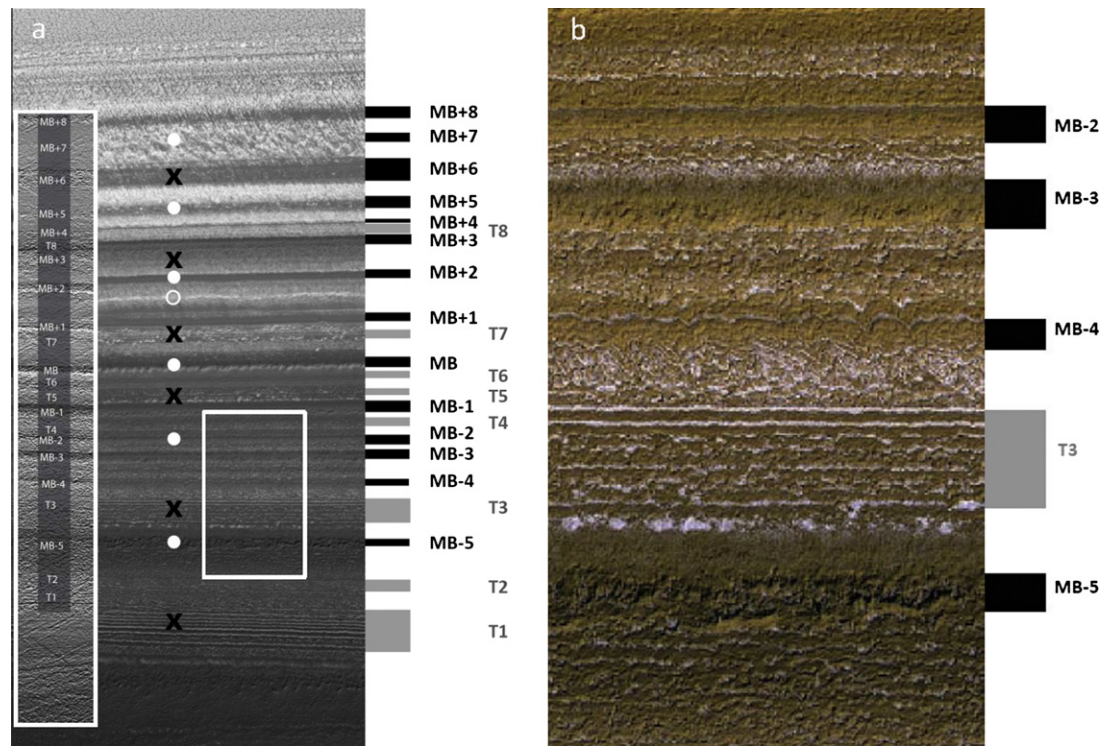
Fig. 3. Portions of HiRISE image PSP_001738_2670 (NASA/JPL/University of Arizona) with indications of marker beds (black) and sections with thin layers (gray) reproduced from the original work (Fishbaugh et al. (2010a)). The layers were identified on a shaded relief map of the trough and two images, see text for further explanation. (a) The visible record of layers in the trough wall with indications of all layers in the stratigraphic column to the right. The layers are labeled according to Fishbaugh et al. (2010a). The inset to the left shows the shaded relief map used to construct the stratigraphic column (Fishbaugh et al. (2010a)). It covers a portion of the trough wall located ~1–2 km from the portion covered by the image. The section marked by a white square is ~640 m wide. (b) Close-up of the section marked by a white square in (a). Interpretation of layers according to our model (Fig. 11) is indicated: Circles indicate layers interpreted to result from low-ice-deposition-rate at high-obliquity with an associated accurate date. The open circle indicates a modelled high-obliquity layer in the model record, not matched by an observed marker bed, but the visible record suggests a layer. Crosses indicate zones formed during periods of peak dust deposition rate.
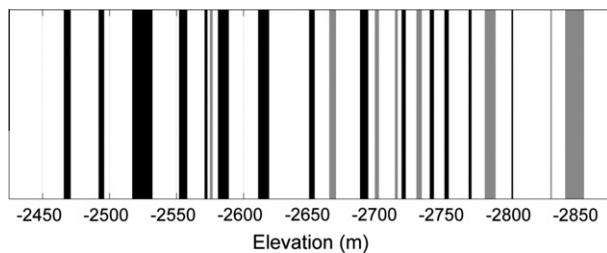

Fig. 4. The observed stratigraphic column, with marker beds (black) and sections with thin layers (gray) indicated (Fishbaugh et al. (2010a)).

chemical composition and size distribution of the dust may also be important. Sequences of marker beds have been correlated between troughs (Fishbaugh and Hvidberg, 2006), and their characteristics must therefore to some extent relate to internal layer properties. We consider here how erosional resistance of layers could relate to their dust content.

Studies of Icelandic glaciers have shown that small concentrations of volcanic ash on a glacier surface may enhance ablation rates due to lower albedo, while a thick layer of ash may have the opposite effect and protect the underlying ice from ablation (Kirkbride and Dugmore, 2003), and a similar mechanism have been proposed for Mars (Head et al., 2003). Sublimation from a dust-rich layer would release dust at the surface, and if not removed by wind and other surface processes, dust may build up and slow down further sublimation. High dust content could also affect the erosional resistance in another way: during formation at the surface, a dusty surface absorbs more solar radiation than

bright surfaces due to lower albedo, and thus becomes warmer in direct sunlight, which could affect the resulting density and consolidation of the layer. A similar effect is known from studies at terrestrial glaciers, where the densification of surface snow depends on temperature (Arthern et al., 2010). When later exposed in a trough wall, densely packed layers are more erosionally resistant than other layers.

The hummocky and pitted texture of marker beds could suggest that these layers are dust-rich, with the erosional resistance being due to very limited ice content, and/or to dust released at the surface and slowing further sublimation. The thin layers could be dust-rich layers that are densely packed due to increased surface temperatures during their formation as described above. Alternatively, their relative smoothness could indicate that they contain less dust than surrounding layers. In any case, the clear topographic distinction of fine layers suggests that there is a significant variation of dust content within the sections with fine layers.

Fig. 3a shows that more layers exist above the highest layer in the stratigraphic record (MB+8), but these layers are covered by perennial ice. We measure an elevation difference of 140 ± 1 m between MB+8 and the horizontal plateau upslope from the trough, which corresponds to the net deposition that has occurred from formation of MB+8 to the present.

If the stratigraphic column can be interpreted to mark layers with a contrast in dust content relative to surrounding layers, it represents a crude climate proxy for Mars during a window of time. With only three different layer types, the record represents an on–off record suggesting that layers form when certain thresholds in the physical properties of the layers are crossed. The distinction of layer types provides additional constraints and

suggests different climate regimes. The interpretation of the record is not directly justified, but critical for its usability to test stratigraphy models, and this will be further discussed below.

4. Climate control of layer formation

We propose a class of climate controlled stratigraphy (CCS) models for formation of the NPLD, where ice and dust are co-deposited, and their respective deposition rates are controlled by climate and vary independently. The net deposition rate at any given time is the sum of ice and dust deposition rates, and the fractional dust content of a layer increment is implied by the respective deposition rates assuming that the layer increment is well mixed.

The concepts of CCS models are illustrated by four simple examples in Fig. 5. Fig. 5a shows an oscillating climate forcing function, Fig. 5b shows four simple examples of climate controlled ice and dust deposition rates, and Fig. 5c shows the four resulting stratigraphies. All four examples have an average dust content of 5% in agreement with observations of the NPLD (Grima et al., 2009). The thickness of a layer increment deposited during a time step Δt is calculated as $(d_{ice} + d_{dust}) \cdot \Delta t$, where d_{ice} and d_{dust} are ice and dust deposition rates during the time of deposition, respectively. The layer thickness is thus in average dominated by the ice deposition rate, as ice is the major constituent, but during time with little or no ice deposition, the resulting layer thickness is dominated by dust deposition rate and thinner layer results. Only in models with temporally uniform ice deposition, the timescale is linearly related to depth (example I). The fractional dust content of a layer increment is calculated as $d_{dust}/(d_{ice} + d_{dust})$, and thus depends linearly on the dust deposition rate, but inversely on the ice deposition rate.

Examples I and II illustrate how variations in ice and dust deposition rates cause different characteristics of the resulting high-dust-fraction layers: Oscillations with amplitudes of 85% of the average ice and dust deposition rates, respectively, result in peak dust fractions of ∼35% and ∼10%, respectively, and high-dust-fraction layers are broad and gradual in example I, and thin and well-defined in example II, respectively. Example III is similar to example II, but here ice deposition rate changes abruptly between a high and a low deposition rate mode when the climate forcing function reaches a threshold value. In the resulting stratigraphy, the high-dust-fraction peaks represent a similar period of time as the lower background level layers between them. Example IV combines examples I and III, and let both ice and dust deposition rates vary, but now with dust deposition rate oscillating in anti-phase with the climate forcing function. The resulting stratigraphy consists of a pattern of broad and thin layers with varying dust content, and illustrates how even a simple climate forcing of ice and dust deposition rates can result in layers of different characteristics and thickness.

The model can create dust lags during times of no ice deposition or even removal of ice, corresponding in the model to $d_{ice} = 0$ or $d_{ice} < 0$, respectively (not illustrated in Fig. 5). If $d_{ice} < 0$, ice from previous time steps is removed, while dust from previous time
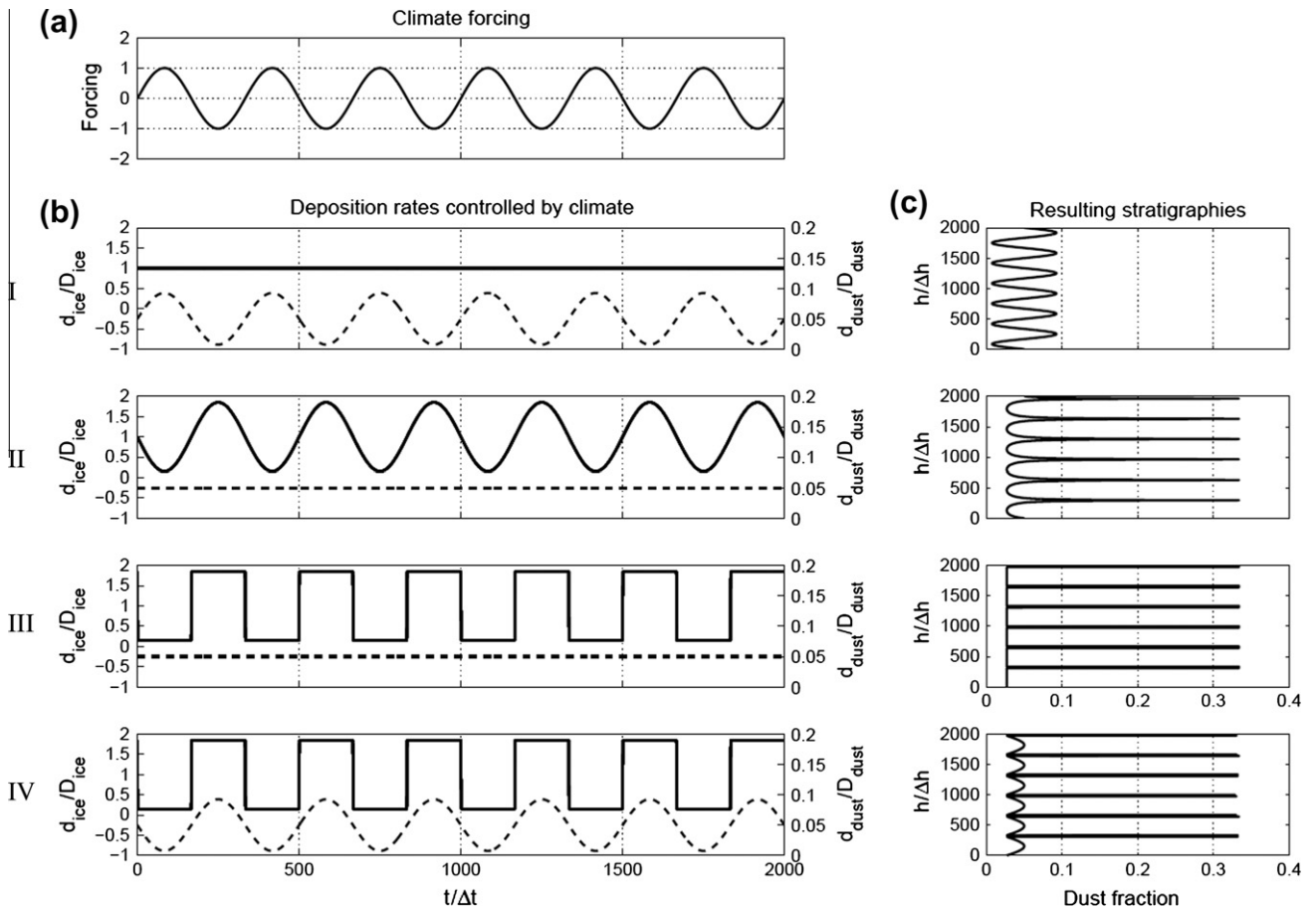

Fig. 5. Figure illustrating the climate controlled stratigraphy (CCS) model concepts for examples I–IV. (a) Climate forcing as a function of time t measured in terms of Δt. (b) Modelled deposition rates of ice d_{ice} (solid) and dust d_{dust} (dashed) controlled by the climate forcing and measured relative to the average deposition rates D_{ice} and D_{dust} of ice and dust, respectively. (c) Resulting model stratigraphy expressed as dust fraction as a function of depth measured in terms of $\Delta h = (D_{ice} + D_{dust}) \cdot \Delta t$. Examples I–IV are discussed in Section 4.

steps remains at the surface and add to the dust deposition at the current time step, to form a dust lag with a fractional dust content of 1.

In this simple model, the fractional dust content is a key property of the stratigraphic record needed to demonstrate the insolation control of martian climate. Fractional dust content is related to climate through climate controlled deposition rates of ice and dust, which also provides the thickness and timescale of the record. To compare the CCS models with observations, we need to derive observable parameters from the model stratigraphy. Some stratigraphic datasets identify individual layers, e.g. the stratigraphic column or radar data. The most significant layers in CCS models are the high-dust fraction peaks (Fig. 5). As a simple first approach, we will assume that model marker beds, i.e. topographically distinct layers, form when the fractional dust content resulting from the CCS model exceeds a certain threshold value. This approach produces a set of model marker beds that can be compared directly to observations assuming that the observed marker beds are dust-rich. It also allows us to distinguish between marker beds formed by low-ice-deposition rates and marker beds formed by high-dust-deposition rates. The threshold for forming layers is not known a priori, but is determined to obtain the best fit between model and data.

5. A physical model of layer buildup

It is now known that the main component of the NPLD is water ice. The bulk dust content is <5% (Grima et al., 2009), but individual layers may contain more dust (Phillips et al., 2008). Different mechanisms for creating layers with higher dust content have been suggested, including formation of dust lags during periods of no ice deposition, or by variations in dust content during ice accumulation (Putzig et al., 2009).

The premise in our work is that layers may have formed by both mechanisms: (1) Water vapor sublimes from the NPLD surface during summer, and precipitates out of the atmosphere during winter. At high obliquity, summer sublimation increases and reduces the net deposition rate or may even remove previously deposited layers, resulting in dust rich deposits. (2) Dust deposition at the NPLD is the result of dust lifting primarily at low latitudes, atmospheric transport and deposition processes. The processes are not fully understood, but atmospheric models suggest that dust raising and transport depend on obliquity, resulting in variations of the polar dust deposition rate.

Our objective here is to express net deposition rates of ice and dust in terms of insolation parameters using the simplest possible expressions that still contain the imprint of insolation cycles on the controlling physical processes. For simplicity, we consider ice and dust deposition independently, and on timescales relevant to insolation cycles ($\sim$10^3 years) we assume that ice and dust co-deposit to form a well-mixed layer increment.

5.1. Ice deposition model

The net annual deposition rate of ice at the North Pole is the result of ice accumulation and ablation processes during the year. It varies significantly over time due to the strong effect of temperature on sublimation rate (Dundas and Byrne, 2010), and climate thus has a direct and strong effect on ablation processes. We assume here that the net annual deposition of ice is the sum of a constant deposition term and a temperature dependent sublimation term.

Sublimation rate depends on $e_{sat} - e$, where e_{sat} is the saturated water vapor pressure over ice, e is the partial pressure of water

vapor in the atmosphere, and e_{sat} is a strong exponential function of temperature T (Schorghofer and Aharonson, 2005), given by:

$$e_{sat}(T) = p_t \exp\left(-\frac{H_{subl}}{R}\left(\frac{1}{T} - \frac{1}{T_t}\right)\right) \quad (1)$$

where p_t = 611 Pa and T_t = 273.16 K are the triple point pressure and temperature, respectively, H_{subl} = 51,058 J mol^{-1} is the molecular heat of sublimation, here assumed constant, and R = 8.314 J K^{-1} mol^{-1} is the universal gas constant.

We calculate monthly (1/12 martian year) averages of the north polar surface temperature $T_i(t)$, $i = 1, \ldots, 12$ over time t from the insolation record (Laskar et al., 2004) using a local energy balance in its simplest form, $\sigma \cdot T^4 = (1 - A) \cdot I$, where σ is the Stefan–Boltzman constant, $I = I(t)$ is time-dependent insolation, we assume a minimum monthly temperature of 150 K and a constant albedo A of 0.4 close to present day values (Byrne et al., 2008), and we neglect other effects from thermal inertia, the atmosphere and from CO_2 frost (Fig. 6b).

Saturated water vapor pressure increases by several orders of magnitude during the summer months, and summer sublimation completely dominates the net annual sublimation. We assume that the monthly mean sublimation rates of ice are approximately proportional to $e_{sat}(T_i)$, $i = 1, \ldots, 12$, implying that the summer sublimation rates dominate, and assuming that e at any time is negligible compared to the summer value of e_{sat}. The proportionality factor depends on wind speed and temperature, but is here assumed constant over time.

We thus express the net annual deposition of ice as a sum of a constant deposition and the monthly mean sublimation rates,

$$d_{ice}(t) = C_1 + C_2 \sum_{i=1}^{12} e_{sat}(T_i(t)) = C_1 + C_2 f(t) \quad (2)$$

where C_1 and C_2 are constants, and f is a function of time t. In order to distinguish between influence from the climate forcing function and other factors, we rearrange the expression to

$$d_{ice}(t) = D_{ice}(1 + A_{ice} \cdot F_{ice}(t)) \quad (3)$$

where D_{ice} is the average annual net deposition rate over the last 1 Myr, A_{ice} is a dimensionless parameter that determines the importance of sublimation, and $F_{ice}(t)$ is a dimensionless function of time t that varies between -1 and 1 with an average of 0 over the last 1 Myr, and expresses the climate controlled part of ice sublimation. It is calculated by

$$F_{ice}(t) = \frac{1}{|\Delta f|_{max}}(f(t) - \langle f \rangle) \quad (4)$$

where $\langle f \rangle$ is the average of $f(t)$ over the last 1 Myr, and $|\Delta f|_{max}$ is the maximum deviation of $f(t)$ from the average during the last 1 Myr. Due to the non-linear dependence of ice deposition on temperature, $F_{ice}(t)$ resembles the step ice deposition function in example III of Fig. 5, with basically constant high deposition rate during low obliquity and dropping to a lower level during high obliquity (Fig. 6d).

5.2. Dust deposition model

The net deposition of dust at the North Pole is the combined result of dust uplift, transport and deposition and involves global scale processes. Atmospheric circulation models have examined dust activity during different orbital conditions, and concluded that obliquity variations have the strongest impact because they affect the meridional temperature gradient, hence both the dust lifting potential and atmospheric transport (Haberle et al., 2003; Newman et al., 2005). However, dust processes, and particularly the role of dust devils, are not yet fully understood on long timescales. At present, dust storms are common near perihelion (northern winter), but during northern winter, CO_2 precipitates
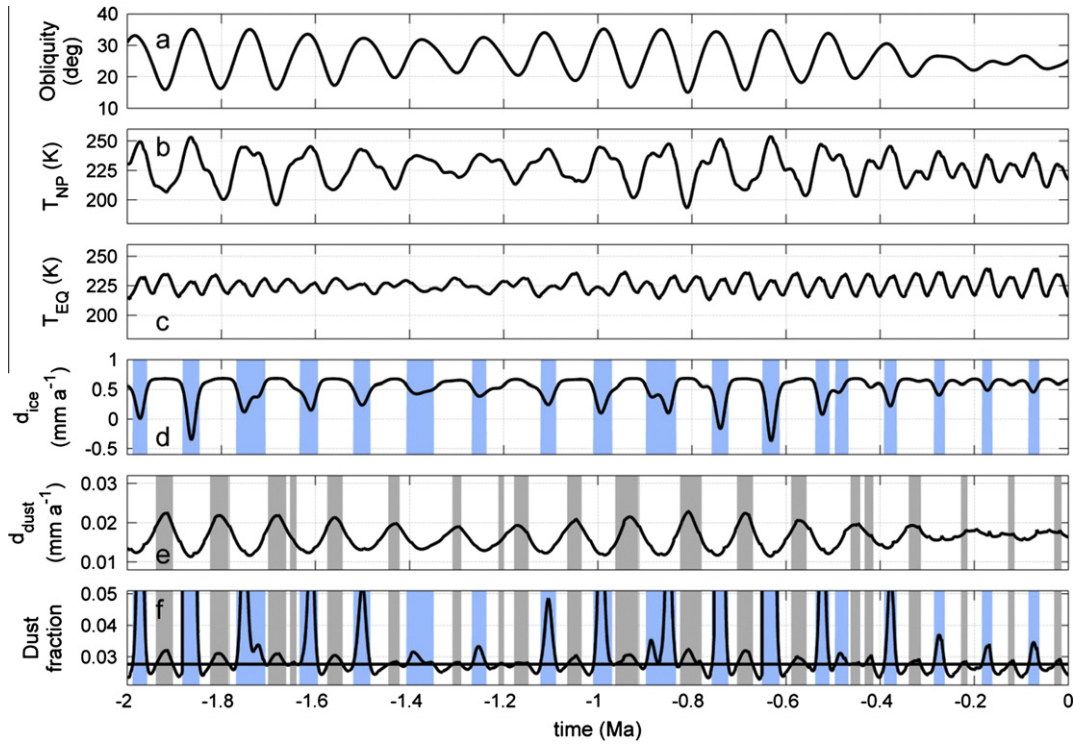
Fig. 6. Climate forcing and modelled deposition rates over the last 2 Myr for the preferred model (D_{ice} = 0.53 mm a^{-1}, A_{ice} = -1.7, A_{dust} = -0.4, B/X = 0.92, X = 3%, δ = 144 m). (a) Obliquity. (b) Maximum monthly mean temperature at the North Pole. (c) Monthly mean temperature at Equator in the month with maximum mean North Polar temperature. (d) Modelled net ice deposition rate. e) Modelled net dust deposition rate. (f) Modelled fractional dust content with the threshold for visible layer formation (horizontal line). Modelled marker beds are indicated by blue and gray lines, with blue lines indicating low-ice-deposition-rate layers formed during high-obliquity and gray lines indicating high-dust-deposition-rate layers formed during low-obliquity. (For interpretation of the references to colour in this figure legend, the reader is referred to the web version of this article.)

out of the atmosphere and removes remaining water ice and dust from the north polar atmosphere (Smith, 2002).

Because of the CO_2 seasonal cycle, we propose that summer conditions are controlling the polar deposition of dust on long timescales. We investigate the effect of insolation forcing by assuming that the annual net deposition of dust is proportional to the monthly mean meridional temperature gradient at North Polar summer solstice, which is essentially an obliquity signal. We write the net annual dust deposition rate as

$$d_{dust}(t) = C_3 + C_4 \Delta T(t) = C_3 + C_4 g(t) \qquad (5)$$

where C_3 and C_4 are constants, $g(t) = \Delta T(t) = T_{NP} - T_{EQ}$ is the monthly average temperature difference between the North Pole and the Equator in the month with maximum average North Polar temperature, and t is time. We calculate monthly (1/12 martian year) averages of temperatures at the North Pole and at the Equator using a local energy balance as described above in Section 5.1, assuming a constant albedo of 0.4 at the North Pole and 0.15 at the Equator, respectively, close to present day values (Byrne et al., 2008) (Fig. 6b and c). As above, we rearrange the expression to

$$d_{dust}(t) = D_{dust}(1 + A_{dust} \cdot F_{dust}(t)) \qquad (6)$$

where D_{dust} is the average annual deposition rate of dust over the last 1 Myr that can be derived from D_{ice} and the average fractional dust content X, which is given by $X = D_{dust}/(D_{dust} + D_{ice})$, i.e. D_{dust} = -$X/(1 - X) \cdot D_{ice}$. A_{dust} is a dimensionless parameter that determines the importance of the insolation forcing, and $F_{dust}(t)$ is a dimensionless function of time t that varies between -1 and 1 with an average of 0 over the last 1 Myr, and expresses the climate controlled part of dust deposition. It is given by

$$F_{dust}(t) = \frac{1}{|\Delta g|_{max}} (g(t) - \langle g \rangle) \qquad (7)$$

where $\langle g \rangle$ is the average of $g(t)$ over the last 1 Myr, and $|\Delta g|_{max}$ is the maximum deviation of $g(t)$ from the average during the last 1 Myr. Due to the essentially linear forcing of dust deposition by obliquity, $F_{dust}(t)$ resembles the simple oscillating dust deposition functions in examples I or IV of Fig. 5, with the sign of the forcing to be discussed below in Section 8.

6. Comparing the model to the stratigraphic column

We have now derived simplified time-dependent expressions of insolation controlled ice and dust deposition rate. The time dependency is expressed by the climate forcing functions $F_{ice}(t)$ and $F_{dust}(t)$, for ice and dust deposition, respectively. A set of only four free model parameters, D_{ice}, A_{ice}, A_{dust}, X, is needed to model the stratigraphy and accumulated layer thickness as a function of time from an initial time in the past according to the CCS model scheme explained in Section 4.

In order to compare the resulting model stratigraphy against the observed stratigraphic column, we must in addition determine a dust fraction threshold B for layer formation (see Section 4) and the elevation offset δ between the top of the model record relative to the top of the stratigraphic column, because it does not extend to present day (Section 3.2). We thus have a set of six free parameters, D_{ice}, A_{ice}, A_{dust}, X, B, δ, to be determined, and we search for the set of parameters that provides the best matching model record to the observed stratigraphic column.

6.1. Search criterion

We need an objective search criterion that takes into account possible discrepancies between the model and the observations. Such discrepancies could arise from several effects: (1) the model neglects variability on cycles shorter than orbital cycles, and this could lead to more observed layers than predicted by our model, (2) layers can only be resolved within the resolution of the observed record, and this could lead to thin layers being absent from the observed record or two layers could appear in the observed record as one merged layer, and (3) random processes or other processes in the climate system could alter the layer formation processes and lead to layers that are too thin or eroded to classify as a marker bed in the observed record.

We formulate a set of criteria that a matching model record should meet. First, the depths of matched modelled and observed layers should fit. Second, the whole sequence of broad and narrow layers should fit, i.e. the modelled and observed layers should overlap with each other, while taking into account that a broad layer in one record could be matched to several narrow layers in the other record as described above. We formulate this as a misfit function J to be minimized:

$$J = \frac{1}{N}\sum_{k=1}^{N}\frac{1}{s^2}(d_k - D_k)^2 + \sum_{j=1}^{T}\left(\frac{1}{2 \cdot l_e}(e_j - E_j)^2 \cdot e_j + \frac{1}{2 \cdot l_E}(e_j - E_j)^2 \cdot E_j\right). \quad (8)$$

The first term compares the depths of observed layers to the nearest observed model layer by a least square method. N is the number of observed layers, d_k and D_k are modelled and observed layer depths of matching layers, respectively, for the kth observed layer, and s is a normalization length. The second term maximizes the overlap between observed layers and model layers over time. The comparison is done over time in order to have equal weight on layers resulting from low ice deposition rates and from high dust deposition. If compared over depth, long periods of no or low ice deposition would not be taken into account. T is the number of time steps considered, e_j and E_j indicates whether the modelled and observed record, respectively, has a layer at the jth time step (no layer = 0, layer = 1), and l_e and l_E is the number of time steps with a layer for the modelled and observed record, respectively.

The second term in the misfit function secures the spacing and thicknesses of layers, and allows broad layers to be matched with several thinner layers, but layer depths are not directly constrained. The first term in the misfit function secures the depths of layers. It generally points to low average net deposition rates, because more densely spaced layers generally provide a better fit. There is no penalty for results with too many model layers, in order to take into account that layers may be missing from the observed record as mentioned above, but thereby limiting the ability to distinguish a good fit. The purpose of using this misfit criterion is to be sure not to exclude a possible good fit due to missing layers in the observed record. The misfit function J is discontinuous over the parameter space because discrete sets of layers are compared.

6.2. Constraining the search

The key parameter of the model stratigraphy is the average deposition rate of ice, D_{ice}, because it controls the rate of NPLD build-up over time. There are only few independent constraints from previous work. Recent crater filling rates provide a maximum constraint of 5 mm a^{-1} over the past 10–20 kyr (Banks et al., 2010), but may not be representative over long timescales. Assuming that the NPLD has been building up over ~5 Myr, as suggested by climate models forced by the insolation record (Levrard et al.,

2007), to the observed thickness of ~2200 m (Phillips et al., 2008), suggests a 5 Myr average net deposition rate of ~0.5 mm a^{-1}. It has been proposed that the NPLD is much older than 5 Myr (Tanaka et al., 2008), and that fine layers corresponds to the obliquity cycle, but our search is limited by the length of the reliably calculated insolation record (Laskar et al., 2004) used to force our model. Since we cannot test this possibility, we focus our search on testing deposition rates that are in agreement with the proposed 5 Myr age of the NPLD. We constrain the search of D_{ice} to be within 0.18 mm a^{-1} and 1.8 mm a^{-1}, i.e. within a factor of 3 of the 5 Myr long-term average net deposition rate (only search results between 0.18 mm a^{-1} and 0.68 mm a^{-1} are shown).

An average net deposition rate of <0.18 mm a^{-1} would imply that top 500 m covered by the stratigraphic column formed in >2.8 Myr. Thus average deposition rates would have been much higher before 2.8 Ma, which seems unlikely given that the polar insolation was generally higher between 5 Ma and 2.8 Ma compared to between 2.8 Ma and present (Fig. 2). An average net deposition rate of >1.8 mm a^{-1} would imply that the visible layers could have built up in <250 kyr, but then insolation cycles would not be important for layer formation, and our model would not be relevant. The range of D_{ice} covers the 0.5 mm a^{-1} proposed by Laskar et al. (2002) from analysis of a brightness profile from the NPLD.

The two parameters A_{ice} and A_{dust}, determining the climate controlled part of deposition rates represent average effects of physical processes that are second order compared to the sublimation physics for ice deposition and the meridional temperature gradient for dust deposition, respectively. According to sublimation physics, A_{ice} must be negative, because high sublimation rates occur at high obliquity. We constrain the search of A_{ice} to be within −3 and +1. The minimum constraint of −3 would result in loss of more than 15 meters of ice during each of the two highest obliquity maxima within the last 1 Myr and would create a dust-rich sublimation lag deposit that could limit further sublimation of ice. Positive values are considered to test the validity and robustness of the sublimation physics above (only search results between −2 and 0 are shown). We constrain the search of A_{dust} to be between −1 and 1, in order to have deposition rate of dust > 0 at all times, but the sign of the forcing is not known.

The average fractional dust content is constrained by radar data to be <5% within the NPLD (Grima et al., 2009). We constrain the search of X to be within 1% and 7% to allow for some uncertainty.

The threshold B of fractional dust content for marker bed formation is not independent of X, because the model stratigraphy must fit a fixed number of marker beds in the stratigraphic column. Internal radar layers are assumed to be dust rich, and dust content of layers of up to 30% have been considered in order to explain observed radar layers (Phillips et al., 2008). If dust is concentrated in thin dust-rich layers, the dust concentration between layers must be close to or less than the bulk content of the NPLD. The visible record contains more layers than the radar record (Phillips et al., 2008), implying that B is close to or less than X. We search for B between 0.4·X and 1.6·X.

The offset δ of the observed stratigraphic column relative to the top of the model record was measured to be 140 m (Section 3.2). We have constrained the search of δ to be within 130 m and 150 m in order to take into account possible effects due to variation in net deposition near troughs or changes in trough geometry after the stratigraphic record formed.

7. Results

We search for the set of parameters that provides the best fit to the observed set of layers according to the search criterion and

constraints, and we perform a systematic search among the constrained parameter space. First, we must consider how to include the two types of layers in the stratigraphic column. The model provides not only a stratigraphy to be compared to the stratigraphic column, but also additional information of the formation mechanism of the layers. However, the model does not include shorter cycles than orbital cycles, and with the constraints on ice deposition rate D_{ice}, it cannot reproduce the sets of thin layers.

As a first approach, we only consider the 14 marker beds, neglect the fine layers, and search for the best fit assuming that these layers are dust-rich. As a second approach, we consider all 22 observed layers, including 14 marker beds and 8 sections with thin layers, and search for the best fit assuming that all these layers are dust-rich. In addition to the search criterion, we use the additional information on the observed layer type (marker bed or section of thin layers) and on the modelled layers (the formation mechanism and fractional dust content) to assess the resulting models.

The analysis is done in three steps:

Step 1: We performed two searches within the constrained parameter space using 14 and 22 observed layers, respectively. The two approaches gave almost similar results with three local minima in the misfit function for D_{ice} around 0.24 mm a^{-1} (model A), 0.42 mm a^{-1} (model B), and 0.52 mm a^{-1} (model C) (Fig. 7 and Table 1). None of these models stand significantly out from other sets of model parameters, suggesting that the misfit criterion is limited in order to allow for possible discrepancies between model and data as discussed above, that our model does not capture some features of the layer characteristics, or the layers do not constrain the model parameters sufficiently. The similar results by the two approaches suggest that including the sections with thin layers do not add more

constraints to the model parameters than already contained in the 14 marker beds. Inspection of the three resulting model stratigraphies for models A–C (Fig. 8) shows that they have significantly different characteristics and chronologies. Model C stands out, because it fits low-ice-deposition-rate layers (identified in the figure as narrow layers with a very high dust fraction) systematically and precisely to observed marker beds, while the two other models fit at least one low-ice-deposition layer to an observed section of thin layers. Model C links high-dust-deposition-rate layers to the remaining observed marker beds and sections with fine layers, but the fit does not show a similar systematic pattern. The broad high-dust-deposition layers are linked to several observed layers (see Table 2 and Fig. 10 for a more detailed comparison).

Step 2: We then investigated model C and its ice-deposition-rate component further. We performed a search within the constrained parameter space using the same misfit criterion as in step 1, but considering only the six marker beds linked to low-ice-deposition layers found in step 1. The purpose is to investigate whether these six layer are sufficient to constrain the timescale. We found one minimum for D_{ice} at 0.52 mm a^{-1} as in step 1, but with a more precise fit to the 6 marker beds, and a lower minima for the misfit than the three models in step 1, A, B and C (Fig. 9 and Table 1). This model has a resulting chronology of layers identical to model C, and $A_{dust} = 0$, i.e. constant dust deposition. This demonstrates that these six marker beds are sufficient to constrain the timescale within the limitations of our model. The model relates these layers to high obliquity maxima with a well-defined age.

Step 3: We did a high-resolution search using all 22 observed layers around model C to investigate the sensitivity of model parameters and refine the fit by specifically searching for models that fit the 6 marker beds. The preferred set of model
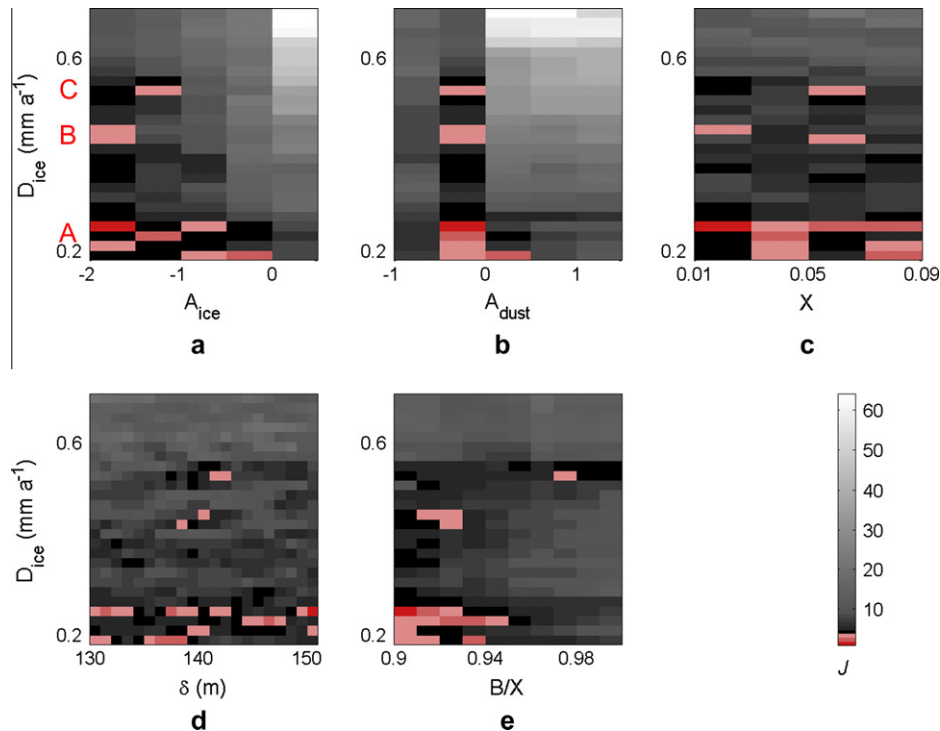

Fig. 7. Step 1: Search results within a constrained range of model parameters showing minimum values of the misfit function J for a fit to all 22 observed layers for (a) combinations of D_{ice} and A_{ice}, (b) combinations of D_{ice} and A_{dust}, (c) combinations of D_{ice} and X, (d) combinations of D_{ice} and δ, (e) for combinations of D_{ice} and B/X. The gray-scale shows values of the misfit function J, with minimum values marked by red. We find local minima with similar low misfit values for three values of D_{ice}: 0.24 mm a^{-1} (A), 0.42 mm a^{-1} (B), and 0.52 mm a^{-1} (C). The sets of parameters for the minima are listed in Table 1, and the resulting stratigraphies are shown in Fig. 8. (For interpretation of the references to colour in this figure legend, the reader is referred to the web version of this article.)

Table 1
Search results.

Search		Results D_{ice} (mm/a)	A_{ice}	A_{dust}	p (%)	B/X (%)	δ (m)	Misfit J
Step 1	(A)	0.24	−2.0	−0.5	1	0.90	150	0.43
	(B)	0.42	−2.0	−0.5	5	0.92	138	0.45
	(C)	0.52	−1.5	−0.5	5	0.97	141	0.45
Step 2		0.52	−0.5	0.0	0	0.99	150	0.39
Step 3		0.53	−1.7	−0.4	3	0.92	144	0.44

Step 1: We searched for models which fit all 22 observed layers (D_{ice} between 0.18 and 1.8 mm a^{-1}), and found three combinations of parameters: models A, B and C (Figs. 7 and 8).
Step 2: We searched for the best fit to six marker beds appointed by model C to be high-obliquity layers.
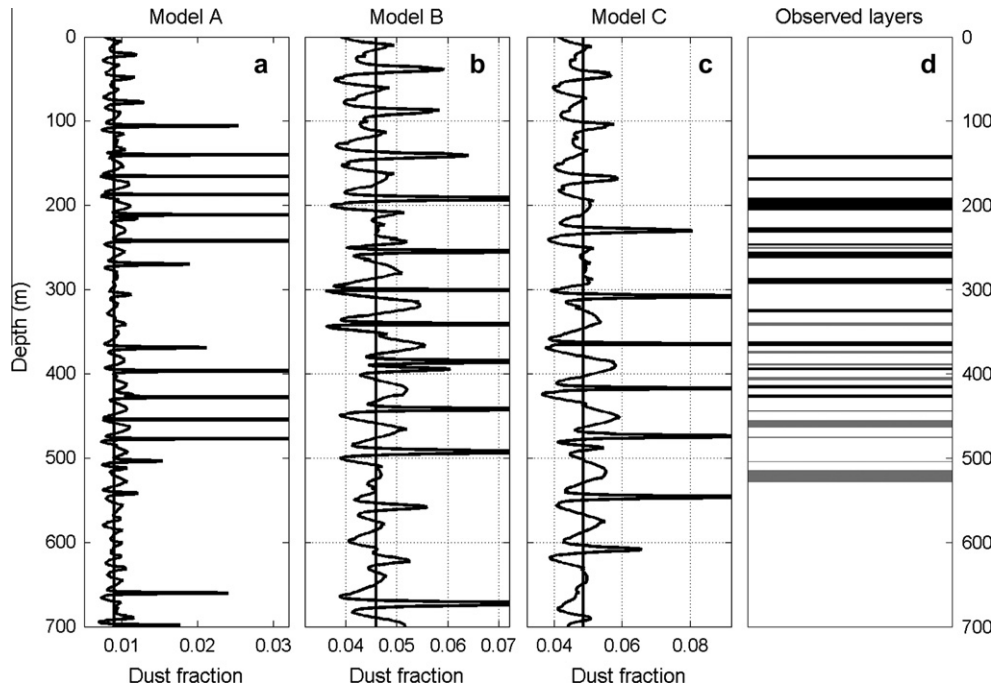Step 3: We performed a high-resolution search near model C and identified the preferred model.

Fig. 8. Step 1: Resulting model stratigraphies for the three models identified by the search shown in Fig. 7 shown as records of fractional dust, and compared to the observed stratigraphic column: (a) model A with D_{ice} = 0.24 mm a^{-1}, (b) model B with D_{ice} = 0.42 mm a^{-1}, (c) model C with D_{ice} = 0.52 mm a^{-1}, and (d) observed stratigraphic column with marker beds (black) and sections of thin layers (gray). The stratigraphic column is shown on a depth scale with the depth of the top layers of 144 m (best fit to model C). The vertical lines in (a–c) mark the model threshold for layer formation. The sets of parameters for the three models are listed in Table 1.

Table 2
Comparison between modelled low-ice-deposition layers and observed marker beds.

Preferred model[a]		Observed[b]		Depth difference (m)
Depth[c] (m)	Age (ka)	Depth[c] (m) (±1 m)	Name	
170.6	274	171.9	MB+7	−1.3
233.2	378	233.0	MB+5	0.2
293.7	482	293.1	MB+2	0.7
311.0[d]	523			
366.4	632	368.0	MB	−1.6
418.0	740	418.5	MB−2	−0.4
480.4	866	478.8	MB−5	1.6

[a] The layers are indicated on the visible stratigraphy in Fig. 1 (white circles).
[b] Depth below surface, i.e. the offset δ = 144 m is added to the observed depths (Fishbaugh et al., 2010a).
[c] Provided for the middle of the layer.
[d] The layer is not matched with an observed marker bed, but the visible stratigraphy suggests a layer not classified as a marker bed (Fig. 3).

parameters is: [D_{ice} = 0.53 mm a^{-1}, A_{ice} = −1.7, A_{dust} = −0.4, X = 3%, B/X = 0.92, δ = 144 m]. The preferred model matches the 22 observed layers according to misfit criterion (Table 1), modelled low-ice-deposition-layers fit 6 observed marker beds

within ±1.6 m (the middle of the layers, Table 2, Fig. 10). It does not uniquely determine the chronology of the stratigraphy, other combinations of parameters near this minimum also match the observed record within the uncertainty and link low-ice-deposition layers to the same set of observed marker beds. The net deposition, however, is similar in all these combinations of parameters. To summarize, the best fit model links six observed marker beds to high-obliquity peaks with a well-defined age (Table 2), it dates the stratigraphic column to extend over time approximately from 990 ka to 200 ka (Table 2, Fig. 10), and it has an average the net deposition rate over this time period of 0.55 mm a^{-1} in agreement with previous estimates (e.g. Laskar et al., 2002).

In order to compare the model stratigraphy directly with the observed data, we constructed a set of model marker beds. However, the continuous model records that underlie the model marker beds contain additional information about the climate conditions. We compare these continuous model records with the observed stratigraphic record to investigate layer formation mechanisms and climate conditions in the different climate regimes suggested by the observed layers (Fig. 11). The comparison shows that all
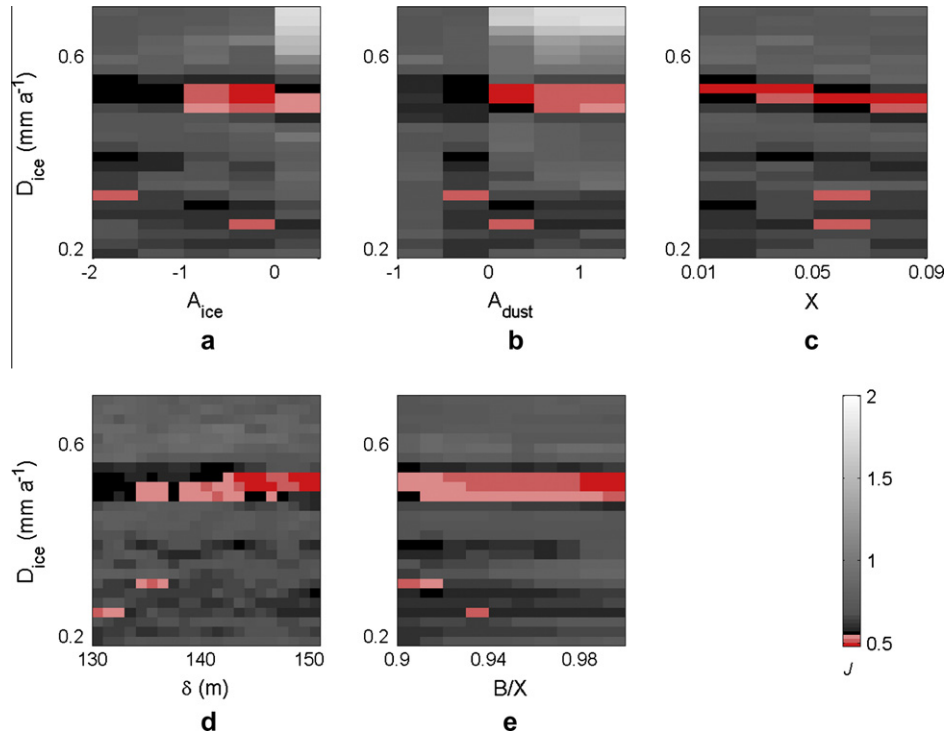
Fig. 9. Step 2: Search results within a constrained range of model parameters showing minimum values of the misfit function *J* for a fit to 6 selected marker beds for (a) combinations of D_{ice} and A_{ice}, (b) combinations of D_{ice} and A_{dust}, (c) combinations of D_{ice} and X, (d) combinations of D_{ice} and δ, (e) for combinations of D_{ice} and B/X. The gray-scale shows values of the misfit function *J*, with minimum values marked by red. We find several local minima as in Fig. 7, but the most significant minimum is now found for $D_{ice} = 0.52$ mm a^{-1}. The set of parameters for this minimum is shown in Table 1. (For interpretation of the references to colour in this figure legend, the reader is referred to the web version of this article.)
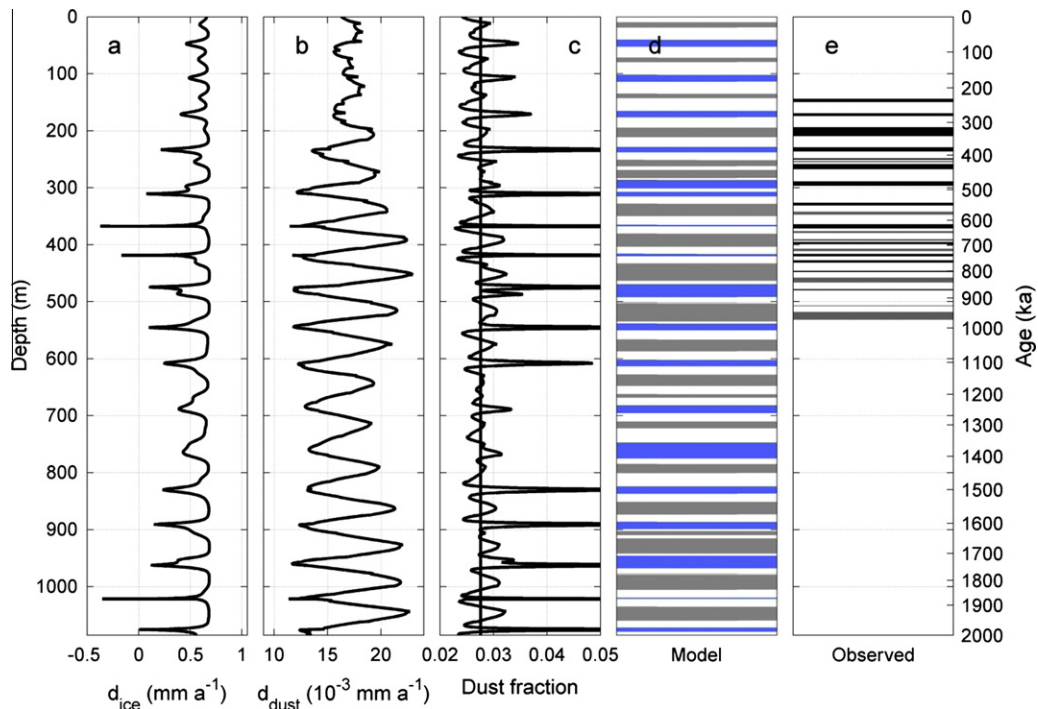

Fig. 10. Modelled stratigraphy 2 Myr back in time for the preferred set of parameters ($D_{ice} = 0.53$ mm a^{-1}, $A_{ice} = -1.7$, $A_{dust} = -0.4$, $B/X = 0.92$, $X = 3\%$, $\delta = 144$ m). (a) Modelled net ice deposition rate. (b) Modelled net dust deposition rate. (c) Modelled fractional dust content with the threshold for layer formation (vertical line) (see the full fractional dust scale between 0 and 1 in Fig. 12c). (d) Modelled marker beds indicated with blue and gray lines, with blue lines indicating low-ice-deposition rate layers formed during high obliquity. (e) Observed stratigraphic column with marker beds (black) and sections with thin layers (gray) plotted on the model depth scale. The model time scale is shown to the right. (For interpretation of the references to colour in this figure legend, the reader is referred to the web version of this article.)
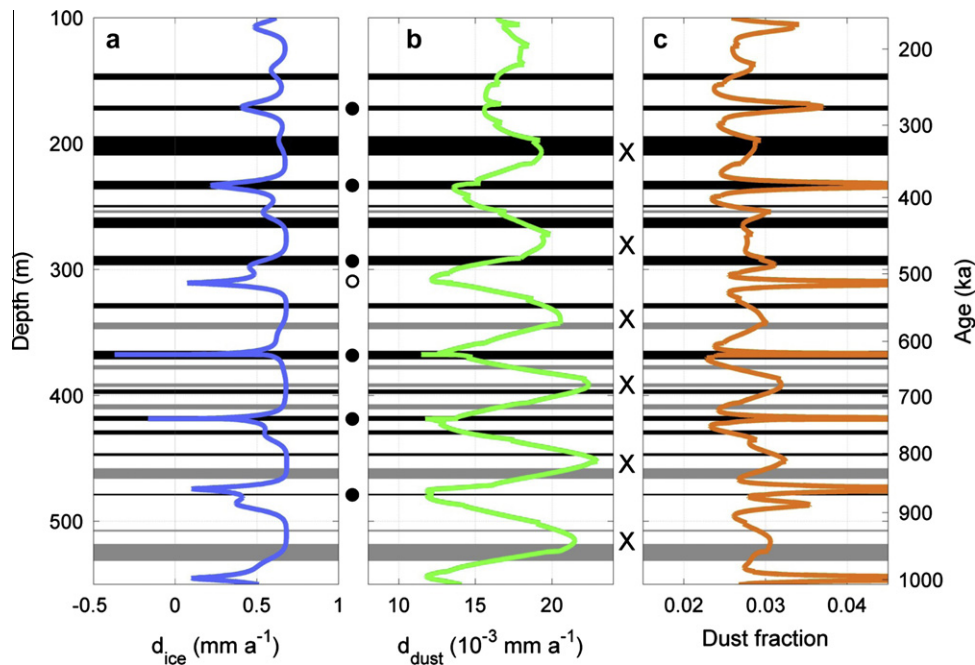
Fig. 11. Comparison between the observed stratigraphic column and the modelled stratigraphy for the preferred set of model parameters (D_{ice} = 0.53 mm a^{-1}, A_{ice} = −1.7, A_{dust} = −0.4, B/X = 0.92, X = 3%, δ = 144 m). (a) Modelled net ice deposition rate. (b) Modelled net dust deposition rate. (c) Modelled fractional dust content (see the full fractional dust scale between 0 and 1 in Fig. 12c). The observed stratigraphic column is indicated on (a–c) with marker beds (black) and sections with thin layers (gray). The model time scale is shown to the right. Filled circles indicate observed marker beds interpreted to be formed due to low ice deposition rate during high obliquity, open circles indicate modelled layers formed due to low ice deposition rate that are not matched with an observed marker bed, but the visible record suggest a layer (Fig. 3a), and crosses indicate zones formed during periods of peak dust deposition rate.

drops in ice deposition rate result in a rise in dust fraction. All dust fraction peaks above ∼0.035 are narrow, due to low-ice-deposition rate and matched with an observed marker bed, except the model layer at 311 m depth (discussed below). Variation in dust fraction between the narrow peaks is gradual with broader maxima, and is due to variation in dust content, sometimes also influenced by minor variations ice deposition rate. The broad maxima are matched with one or several observed marker beds and/or sections of thin layers, but the match is not as precise as for the dust fraction peaks, and the model dust fraction between the narrow peaks is missing finer structures present in the observed stratrigraphic column.

We mark the observed marker bed formed due to a low-ice-deposition-rate by circles, and the depths of maximum dust deposition rate by crosses (Fig. 11). The sequence of marks emphasize that the layer formation mechanism according to the best fit model alternates between layers formed by low-ice-deposition-rate at high obliquity and layers formed by high-dust-deposition-rate at low obliquity. The marks were transferred to the visual image to illustrate the relation between model records, the stratigraphic record and the visual appearance of layers. Comparison with the visual image provides further information. One modelled low-ice-deposition marker bed (311.0 m depth) is not matched with a marker bed. The visual image shows, however, a distinct, bright layer at a corresponding depth, but the layer is thin and not as regular as the other marker beds (Fig. 3a), and it did not have a measurable topographic relief. The broad model marker bed at 480.4 m depth contains a double peak in dust fraction, but only one marker bed was observed.

8. Discussion

The net deposition rates of ice and dust determined by our model represent the average net deposition rates over >1 kyr

timescales and they may differ significantly from current deposition rates. The model predicts a current net accumulation rate over the past 1 kyr to be 0.7 mm a^{-1}, generally consistent with the upper limit of resurfacing rate over the last 10–20 kyr of 3–4 mm a^{-1} (Banks et al., 2010). The model does include formation of disconformities at periods with no or negative ice deposition (net sublimation). In the model such disconformities result in formation of marker beds. Surface roughness of the NPLD may influence the spatial distribution of deposition and sublimation of ice and dust at a given time. On longer timescales it may potentially lower the resolution of the stratigraphic record by disrupting thin layers that will then appear to be missing from the observed stratigraphy.

The preferred model had a negative A_{dust}, i.e. within the model, dust deposition rate is high at low obliquity (Fig. 6). Dust lifting by wind stress increases with increasing obliquity as the meridional wind circulation strengthens (Haberle et al., 2003; Newman et al., 2005). However, atmospheric circulation models suggest that polar dust deposition rates due to dust devil lifting increase with decreasing obliquity below 25°, and that polar dust deposition at low obliquities may be increasingly due to dust lifted by dust devils (Newman et al., 2005). The modelled high-dust-deposition-rate layers forming at low obliquity could suggest that dust devils have an important role on long time scales.

The modelled high-dust-deposition layers are often broad, they do not match marker beds as accurately as the low-ice-deposition layers, and they are often matched with several marker beds and sections of thin layers (Fig. 10). The additional structure in the stratigraphic column suggests that our dust deposition scheme does identify layers with high dust activity, but it is too simple and does not catch the shorter cycle variations that may be related to dust processes. In the search, we assumed that sections with fine layers were dust-rich. More complicated dust schemes could accommodate alternative interpretations of the sections with fine layers and still provide the same overall chronology.

The record of marker beds resulting from the preferred model, shown in Fig. 10d, has 16–18 model marker beds per 500 m depth, suggesting that the preferred model stratigraphy contains a quasi-periodic cycle of ~30 m wavelength. The model marker beds are resulting from a combination of layers produced by low-ice-deposition-rate at high obliquity and high-dust-deposition-rate at low obliquity, similar to the simple example IV (Fig. 5). The signal corresponds to half of the obliquity cycles of 120 kyr and 99 kyr (Laskar et al., 2004), that influences both ice and dust deposition rates, and not the precession cycle of 51 kyr as previously proposed (Laskar et al., 2002; Milkovich and Head, 2005).

We compare the preferred model to other observations from the NPLD:

– The most significant sublimation lag in the modelled record with a loss of 4 m of ice occurred at an obliquity peak at 632 ka and matches the original marker bed (Malin and Edgett, 2001) ("MB", Fig. 3a), which is the most prominent layer in the visible record.
– The fractional dust content of low-ice-deposition-rate layers is significantly higher than elsewhere, and if we extend the reconstruction back in time, we find no peak dust content layers at depths between approximately 600 m and 820 m (Fig. 10)

corresponding to a low-amplitude-obliquity period at 1.1–1.5 Ma (Fig. 2). The depth interval matches approximately the depths of an echo-free zone in radar images (Phillips et al., 2008; Putzig et al., 2009) (Fig. 12).

– Assuming that the expressions for ice and dust deposition rates are unchanged back in time, we have run the stratigraphy model through 10 Myr forced by the insolation record (Fig. 2) to simulate the build-up of the NPLD (Fig. 12). The simulation assumes that the net deposition rates of ice and dust vary due to the insolation, while all model parameters remain constant through time. To avoid a steady build up of pure dust at times with no ice, we assume that dust only remains on the surface if ice is present beneath. The simulation suggests that the NPLD started to build up at 4.2 Ma, in agreement with results of a global climate model (Levrard et al., 2007), and provides a modelled present thickness of 2407 m, comparable to the observed thickness of ~2200 m (Phillips et al., 2008). We compare the modelled fractional dust record with the observed internal radar layer structure at the approximate location of the stratigraphic column (marked by the gray line in Fig. 12). Model layers with high fractional dust content are structured in packages, similar to the observed internal radar layer structure (Fig. 12), and suggesting a scenario where the three modelled packages
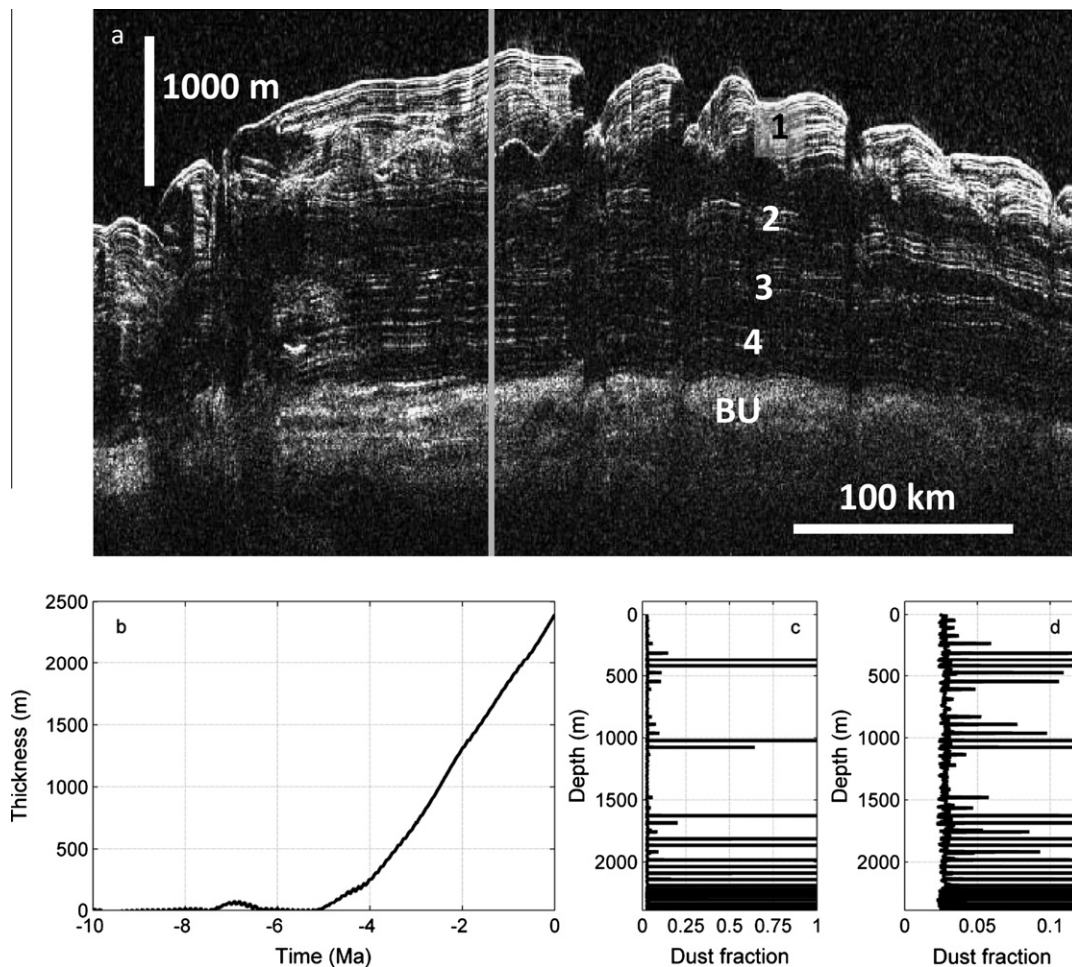

Fig. 12. (a) Radargram from the SHARAD instrument on Mars Reconnaissance Orbiter showing the internal stratigraphy of the NPLD with packages of layers separated by zones of no reflectors (Phillips et al., 2008). The Basal Unit underlying the NPLD (BU) and four layer packages (1–4) are labeled according to Phillips et al. (2008). The approximate location of the stratigraphic column is marked by the gray line. (Image Credit: NASA/JPL-Caltech/University of Rome/SwRI). (b) Modelled evolution of the NPLD during the last 10 Myr showing the thickness of the NPLD as a function of time. (c) The modelled stratigraphy for the preferred set of model parameters (D_{ice} = 0.53 mm a^{-1}, A_{ice} = −1.7, A_{dust} = −0.4, B/X = 0.92, X = 3%, δ = 144 m) plotted as fractional dust content as a function of depth. (d) As (c), but zooming in on dust fraction content below 12%. The modelled thickness of the NPLD is 2407 m.

of high fractional dust peaks (approximate modelled depths of above 600 m, around 1000 m, and below 1500 m), correspond to radar layer packages labeled 1, 2, and 3 and 4 together, respectively. The radar layers seem to correlate with low-ice-deposition layers formed at high obliquity as previously suggested (Phillips et al., 2008), and future studies should investigate this relation further.

9. Conclusion

We have developed a model for building up the NPLD and creating its stratigraphy. The model is based on the physical processes that relate insolation forcing to climate and deposition rates of ice and dust, and allows for investigation of the climate control of NPLD stratigraphy.

The model was compared to a previously published quantitative stratigraphic column (Fishbaugh et al., 2010a), and a preferred set of model parameters were determined by a best fit of the modelled stratigraphy to the set of observed layers. The preferred model provides a consistent explanation of layer formation and build-up of the NPLD, and has a net deposition rate of 0.55 mm a^{-1}. It matches six observed marker beds in the stratigraphic column with model layers formed by low-ice-deposition-rate at high obliquity within ±1.6 m. The six layers are linked to high-obliquity peaks with a well-defined age and date the top 500 m of the NPLD to approximately 1 Ma. Within the model, fine layers in the stratigraphic column are related to periods with high dust deposition rate. The fine layers and additional structure in the stratigraphic record occurring during periods of high dust deposition rates were not reproduced by our model, and suggest that our dust deposition scheme is too simple and does not catch shorter cycle variations. Future studies may explore more complex dust deposition schemes.

The preferred model stratigraphy contains a quasi-periodic ∼30 m cycle, similar to a previously suggested cycle in brightness profiles from the NPLD (Laskar et al., 2002; Milkovich and Head, 2005), but here related to half of the obliquity cycles of 120 ka and 99 kyr and resulting from a combination of ice and dust deposition processes that both vary with obliquity cycles.

The comparison with other observations from the NPLD demonstrates that the preferred model is plausible, but it does not provide a rigorous test of whether it is correct. The validity of the preferred model to constrain NPLD chronology is limited by several factors. The interpretation of the stratigraphic column as a proxy for the dust content lacks proper justification, although a relation is proposed where marker beds and thin layers are dust-rich. The fine layers in the stratigraphic column represent an important part of the stratigraphy, but they cannot be adequately reproduced by the model. The search for model parameters was limited to investigate deposition rates consistent with a build up over approximately 5 Myr. It has been proposed that the NPLD is much older than 5 Myr (Tanaka et al., 2008). It would require formation of dust lags to effectively protect the cap against sublimation during long periods of high obliquity, possibly inconsistent with the low bulk dust content of the NPLD (Putzig et al., 2009), but this scenario cannot be tested within the current model due to the limited length of a reliable insolation record (Laskar et al., 2004).

The model presented here proposes a link between the NPLD stratigraphy and insolation cycles based on physical processes. More work is needed to constrain the chronology of NPLD layers and investigate the climate control of the NPLD. Future studies should include records from other geographical locations to assess the spatial variation of this relation and other stratigraphic data that could provide additional constraints.

Appendix A. Supplementary material

Supplementary data associated with this article can be found, in the online version, at http://dx.doi.org/10.1016/j.icarus.2012.08.009. These data include Google maps of the most important areas described in this article.

References

Arthern, R.J., Vaughan, D.G., Rankin, A.M., Mulvaney, R., Thomas, E.R., 2010. In situ measurements of Antarctic snow compaction compared with predictions of models. J. Geophys. Res. 115, F03011. http://dx.doi.org/10.1029/2009JF001306.

Banks, M.E. et al., 2010. Crater population and resurfacing of the martian north polar layered deposits. J. Geophys. Res. 115, E08006. http://dx.doi.org/10.1029/2009JE003523.

Byrne, S., Zuber, M.T., Neumann, G.A., 2008. Interannual and seasonal behaviour of martian residual ice-cap albedo. Planet. Space Sci. 54, 194–211.

Clifford, S.M. et al., 2000. The state and future of Mars polar science and exploration. Icarus 144, 210–242.

Cutts, J.A., Lewis, B.H., 1982. Models of climate cycles recorded in martian polar layered deposits. Icarus 50, 216–244.

Dundas, C.M., Byrne, S., 2010. Modeling sublimation of ice exposed by recent impacts in the martian Mid-Latitudes. Icarus 206 (2), 716–728.

Fishbaugh, K., Hvidberg, C., 2006. Martian north polar layered deposits stratigraphy: Implications for accumulation rates and flow. J. Geophys. Res. 111 (E06012). http://dx.doi.org/10.1029/2005JE002571.

Fishbaugh, K.E., Hvidberg, C.S., Beaty, D., Clifford, S., Fisher, D., Haldemann, A., Head, J.W., Hecht, M., Koutnik, M., Tanaka, K., Ammamm, W.J., 2008. Introduction to the 4th Mars polar science and exploration conference special issue: Five top questions in Mars polar science. Icarus 196, 305–317.

Fishbaugh, K.E., Hvidberg, C.S., Byrne, S., Russel, P.S., Herkenhoff, K.E., Winstrup, M., Kirk, R., 2010a. The first high-resolution stratigraphic column of the martian north polar layered deposits. Geophysical Research Letters 37, L07201. http://dx.doi.org/10.1029/2009GL041642.

Fishbaugh, K.E., Byrne, S., Herkenhoff, K., Kirk, R., Fortezzo, C., Russell, P., McEwen, A., 2010b. Evaluating the meaning of "layer" in the martian north polar layered deposits and the impact on the climate connection. Icarus 205, 269–282.

Grima, C. et al., 2009. North polar deposits of Mars: Extreme purity of the water ice. Geophys. Res. Lett. 36, L03203. http://dx.doi.org/10.1029/2008GL036326.

Haberle, R.M., Murphy, J.R., Schaeffer, J., 2003. Orbital change experiments with a Mars general circulation model. Icarus 161, 66–89.

Hays, J.D., Imbrie, J., Shackleton, N.J., 1976. Variations in the Earth's orbit: Pacemaker of the ice ages. Science 194, 1121–1132.

Head, J.W., Mustard, J.F., Kreslavsky, M.A., Milliken, R.E., Marchant, D.R., 2003. Recent ice ages on Mars. Nature 426, 797–802. http://dx.doi.org/10.1038/nature02114, 6968.

Herkenhoff, K., Byrne, S., Russell, P., Fishbaugh, K., McEwen, A., 2007. Meter-scale morphology of the north polar region of Mars. Science 317, 1711–1715.

Howard, A., Cutts, J., Blasius, K., 1982. Stratigraphic relationships within the martian polar cap deposits. Icarus 50, 161–215.

Ivanov, A.B., Muhleman, D.O., 2000. The role of sublimation for the formation of the Northern ice cap: Results from the Mars Orbiter Laser Altimeter. Icarus 144, 436–448.

Kirkbride, M.P., Dugmore, A.J., 2003. Glaciological response to distal tephra fallout from the 1947 eruption of Hekla, south Iceland. J. Glaciol. 49 (166), 420–428. http://dx.doi.org/10.3189/172756503781830575.

Laskar, J., Levrard, B., Mustard, J., 2002. Orbital forcing of the martian polar layered deposits. Nature 419, 375–377.

Laskar, J., Correia, A.C.M., Gastineau, M., Joutel, F., Levrard, B., Robutel, P., 2004. Long term evolution and chaotic diffusion of the insolation quantities of Mars. Icarus 170, 343–364.

Levrard, B., Forget, F., Montmessin, F., Laskar, J., 2007. Recent formation and evolution of northern martian polar layered deposits as inferred from a global climate model. J. Geophys. Res. 112, E06012. http://dx.doi.org/10.1029/2006JE002772.

Malin, M., Edgett, K., 2001. Mars global surveyor Mars Orbiter Camera: Interplanetary cruise though primary mission. J. Geophys. Res. 106 (E10), 23,429–423,570.

Milkovich, S., Head, J.W., 2005. North polar cap of Mars: Polar layered deposit characterization and identification of a fundamental climate signal. J. Geophys. Res. 110 (E05). http://dx.doi.org/10.1029/2004JE002349.

Milkovich, S., Head, J.W., Neukum, G., the HRSC Co-Investigator Team., 2008. Stratigraphic analysis of the northern polar layered deposits of Mars: Implications for recent climate history. Planet. Space Sci. 56, 266–288.

Murray, B.C., Soderblom, L.A., Cutts, J.A., Sharp, R.P., Milton, D.J., Leighton, R.B., 1972. Geological framework of the south polar layered region of Mars. Icarus 17, 328–345.

Newman, C.E., Lewis, S.R., Read, P.L., 2005. The atmospheric circulation and dust activity in different orbital epochs on Mars. Icarus 174, 135–160. http://dx.doi.org/10.1016/j.icarus.2004.10.023.

Perron, J., Huybers, P., 2009. Is there an orbital signal in the polar layered deposits on Mars? Geology 37 (2), 155–158.

Phillips, R. et al., 2008. Mars north polar deposits: Stratigraphy, age, and geodynamical response. Science 320 (5880), 1182–1185. http://dx.doi.org/10.1126/science.1157546.

Putzig, N., Phillips, R., Campbell, B., Holt, J., Plaut, J., Carter, L., Egan, A., Bernardini, F., Safaeinili, A., Seu, R., 2009. Subsurface structure of planum boreum from Mars reconnaissance orbiter shallow radar soundings. Icarus 204, 443–457.

Schorghofer, N., Aharonson, O., 2005. Stability and exchange of subsurface ice on Mars. J. Geophys. Res. 110, E05003. http://dx.doi.org/10.1029/2004JE002350.

Smith, M.D., 2002. The annual cycle of water vapor on Mars as observed by the Thermal Emission Spectrometer. J. Geophys. Res. 107, 5115. http://dx.doi.org/10.1029/2001JE001522.

Smith, I.B., Holt, J.W., 2010. Onset and migration of spiral troughs on Mars revealed by orbital radar. Nature 465. http://dx.doi.org/10.1038/nature09049.

Tanaka, K.L., 2005. Geology and insolation-driven climatic history of Amazonian north polar materials on Mars. Nature 437. http://dx.doi.org/10.1038/nature04065.

Tanaka, K., Rodriguez, J., Skinner, J., Bourke, M., Fortezzo, C., Herkenhoff, K., Kolb, E., Okubo, C., 2008. North polar region of Mars: Advances in stratigraphy, structure, and erosional modification. Icarus 196 (2), 305–317.

Toon, O.B., Pollack, J.B., Ward, W., Burns, J.A., Bilski, K., 1980. The astronomical theory of climatic changes of Mars. Icarus 44, 552–607.